nature physics

Article

https://doi.org/10.1038/s41567-023-02065-9

Nonlinear nanomechanical resonators approaching the quantum ground state

In the format provided by the authors and unedited

Supplementary Information

Contents

I. THEORETICAL DESCRIPTION

A. Structure of the section

This section provides the basic theoretical description of the problem. It is structured as follows. In Sec. I B we will first recall the standard description of incoherent transport in a single-electron transistor. We then derive in Sec. I C the back-action of the electronic transport on the oscillator, obtaining an expression for the damping coefficient and the quadratic coefficient of the effective potential. In Sec. I D we derive in the equilibrium case the full non-linear effective potential of the oscillator. We obtain ω_Q from the quadratic term of the effective potential. In Sec. I E we derive the displacement fluctuation spectrum $S_{xx}(\omega)$ for the oscillator at equilibrium and discuss its behaviour. In Sec. I F we derive expressions for the first four coefficients in the expansion in the displacement x of the effective potential and the average of the full non-linearity. In Sec. I G we recall the main steps of the derivation of the Fokker-Planck equation for the oscillator quadratures in a Duffing description of the response to a drive. We then describe how we have used its numerical solution to fit the observed nonlinear spectra (Sec. I H). We use ω_0 instead of ω_m^o for the bare resonance frequency to make the expressions more compact.

B. Electronic transport

Electronic transport measurements in the device are described by incoherent tunnelling in the Coulomb blockade regime. This corresponds to the condition $\hbar\Gamma_{\mathrm{e}} \ll k_B T \ll \Delta E \ll E_C$, where Γ_{e} is the tunneling rate of the electrons to the quantum dot, $E_C = e^2/C_\Sigma$ is the Coulomb energy (C_Σ the total capacitance of the dot, ΔE the electronic level spacing, e the electron charge). For a description of transport in this regime see for instance Ref. [1]. Concerning the oscillator we found that the system lays in the regime $\hbar\omega_0 \ll \hbar\Gamma_{\mathrm{e}} \ll k_B T$, where we recall that ω_0 is the (bare) mechanical resonance frequency measured far from the conductance peaks. This implies that the oscillator can be described by a classical approach and that it is much slower than the electronic degrees of freedom. We will use then a Born-Oppenheimer kind of approximation, where one first solves the electronic problem for a given value of the displacement x of the oscillator and then considers the back-action of the electronic system on the oscillator [2–6].

We begin with the electronic description for the case of N_s electronic degrees of freedom, where $N_s = 1$ describes the spinless case, $N_s = 2$ the spin- or valley-degenerate case, and $N_s = 4$ the case when both valley and spin degeneracy are taken into account. We will find that most results do not depend on the actual value of N_s. In the incoherent transport regime ($k_B T \gg \hbar\Gamma_{\mathrm{e}}$) the system is fully described by the probability that the electronic state σ (for instance σ could be the spin projection) is occupied: P_σ. We define also the probability that the dot is empty P_0, or occupied by one of the σ states $P_1 = \sum_\sigma P_\sigma$. We assume that Coulomb blockade forbids double occupancy of the dot. One can then write a Pauli master equation for these probabilities:

$$\dot{P}_\sigma = \Gamma^+ P_0 - \Gamma^- P_\sigma. \tag{1}$$

Here $\Gamma\pm = \Gamma_L^\pm + \Gamma_R^\pm$, and $\Gamma_\alpha^\pm$ is the rate at which an electron is added (+) or removed (−) from the quantum dot from the α (=L, R) lead. The probability satisfies the sum-rule $\sum_\sigma P_\sigma + P_0 = 1$. The explicit expression of the rates depends on the Fermi distributions on the leads: $\Gamma_\alpha^+ = \Gamma_\alpha f_\alpha$ and $\Gamma_\alpha^- = \Gamma_\alpha(1 - f_\alpha)$, where by symmetry the rates do not depend on σ. The electric current at the left lead and going from the left to the right lead, reads then:

$$I_L = -e\left[N_s\Gamma_L^+(1-P_1) - \Gamma_L^- P_1\right] \tag{2}$$

where we introduced the probability that the dot is occupied with one electron of any species $P_1 = \sum_\sigma P_\sigma$. The equation of motion for the probability simplifies to

$$\dot{P}_1 = N_s\Gamma^+ - (N_s\Gamma^+ + \Gamma^-)P_1. \tag{3}$$

Using its stationary solution one finds that the current is

$$I_L = -eN_s(\Gamma_R^-\Gamma_L^+ - \Gamma_L^-\Gamma_R^+)/\Gamma_\mathrm{e}, \tag{4}$$

where $\Gamma_\mathrm{e} = N_s\Gamma^+ + \Gamma^-$. Setting the right lead to the ground as in the experiment and using V_g and V as the voltage potentials applied to the gate and the left lead, one can write the dependence of the Fermi distributions on these voltages: $f_L = f_F(\epsilon_1 - e(V_g - V)C_g/C_\Sigma + eVC_R/C_\Sigma)$ and $f_R = f_F(\epsilon_1 - eV_gC_g/C_\Sigma - eVC_R/C_\Sigma)$, where C_L, C_R, C_g are the left, right and gate capacitances, $C_\Sigma = C_L + C_R + C_g$, $f_F(\epsilon) = 1/(e^{\epsilon/k_BT}+1)$, and $\epsilon_1 = \epsilon_0 + (e^2 - 2Qe)/2C_\Sigma$, with Q the total charge on the dot, and ϵ_0 the single electron energy.

We can now calculate the conductance for vanishing bias voltage:

$$G = -\frac{\Gamma_L\Gamma_R N_s e^2}{(\Gamma_L+\Gamma_R)[1+(N_s-1)f_0]}\frac{\partial f_0}{\partial \epsilon_1} \tag{5}$$

where we introduced $f_0 = f_L = f_R$ for $V = 0$. The conductance has a maximum when the argument of the Fermi function equals $k_BT\ln N_s/2$.

C. Back-action on the oscillator

We now consider the coupling of the quantum dot to the oscillator. When one electron is added to the dot, an additional electrostatic force F_e acts on the oscillator leading to a term in the Hamiltonian $-F_exn$, where n is the additional number of electrons on the dot. In the incoherent regime n can only take the integer values 0 or 1. (In the main text we used the usual notation found in the opto-mechanical literature for the coupling $\hbar g = F_e x_\mathrm{zp}$, where $x_\mathrm{zp} = \sqrt{\hbar/2m\omega_0}$ with m the mass of the oscillator.) The presence of this coupling term changes the previous equations in Sec. I B by introducing the following substitution in the rate expressions:

$$\epsilon_0 \to \epsilon_0 - F_e x. \tag{6}$$

We can then write a system of equations describing the oscillator position and the probability of occupation of the dot [7]:

$$\begin{aligned} m\ddot{x} &= -m\omega_0^2 x - m\gamma\dot{x} + F_eP_1(t) + F(t) && (7)\\ \dot{P}_1(t) &= N_s\Gamma^+(x) - \Gamma_\mathrm{e}(x)P_1, && (8)\end{aligned}$$

here γ and $F(t)$ are the intrinsic damping rate and a weak external force driving the oscillator.

Assuming small displacements from the equilibrium value of both x and P_1 we can define

$$\begin{aligned} x &= x_0 + \tilde{x}(t) && (9)\\ P_1 &= P_1^{(0)} + \tilde{P}_1(t). && (10)\end{aligned}$$

We obtain the following non-linear equations for x_0 and $P_1^{(0)}$:

$$\begin{aligned} x_0 &= \frac{F_e}{m\omega_0^2}P_1^{(0)} && (11)\\ P_1^{(0)} &= \frac{N_s\Gamma^+(x_0)}{\Gamma_\mathrm{e}(x_0)}, && (12)\end{aligned}$$

and a linear system for the small fluctuating parts $\tilde{x}$ and $\tilde{P}_1$:

$$\begin{aligned} \ddot{\tilde{x}} &= -\omega_0^2\tilde{x} - \gamma\dot{\tilde{x}} + (F_e/m)\tilde{P}_1 + F(t)/m && (13)\\ \dot{\tilde{P}}_1 &= [N_s\partial_x\Gamma^+ - P_1^{(0)}\partial_x\Gamma_\mathrm{e}]\tilde{x} - \Gamma_\mathrm{e}\tilde{P}_1. && (14)\end{aligned}$$

Introducing the Fourier transform $\tilde{x}(\omega) = \int dte^{i\omega t}\tilde{x}(t)$ and using the explicit form of $P_1^{(0)}$ we have:

$$\tilde{P}_1(\omega)(\Gamma_\mathrm{e} - i\omega) = N_s(\Gamma^-\partial_x\Gamma^+ - \Gamma^+\partial_x\Gamma^-)\tilde{x}(\omega). \tag{15}$$

Substituting this expression into the equation for the displacement we have

$$[-\omega^2 + \omega_Q^2 - i\omega\gamma_R]\tilde{x}(\omega) = F(\omega)/m \tag{16}$$

with the renormalized damping and frequency:

$$\begin{aligned} \gamma_R &= \gamma - \frac{F_e^2N_s}{m\Gamma_\mathrm{e}}\Xi, && (17)\\ \omega_Q^2 &= \omega_0^2 + \frac{F_e^2N_s}{m}\Xi, && (18)\end{aligned}$$

where we use the notation ω_Q since it is related to the quadratic coefficient of the effective potential. We defined

$$\Xi = \frac{\Gamma^-\partial_{\epsilon_1}\Gamma^+ - \Gamma^+\partial_{\epsilon_1}\Gamma^-}{\omega^2 + \Gamma_\mathrm{e}^2}. \tag{19}$$

More explicitly, we have:

$$\Xi = -\frac{1}{k_BT}\frac{(\Gamma_L+\Gamma_R)[\Gamma_Lf_L(1-f_L) + \Gamma_Rf_R(1-f_R)]}{\omega_0^2 + \Gamma_\mathrm{e}^2}, \tag{20}$$

where we substituted ω by the value of the unperturbed resonance frequency ω_0. Strictly speaking when the reduction of ω_Q is large one should insert ω_Q and obtain a self-consistent equation, but since we are interested in the limit of $\Gamma \gg \omega_0 > \omega_Q$ this will have a negligible impact on the final result. The expression simplifies further in the relevant limit $eV \ll k_BT$ used in the experiment:

$$\Xi = -\frac{1}{k_BT}\frac{(\Gamma_L+\Gamma_R)^2f_0(1-f_0)}{\omega_0^2 + (\Gamma_L+\Gamma_R)^2[1+(N_s-1)f_0]^2}, \tag{21}$$

where $f_0 = f_L = f_R$ is the Fermi distribution of the leads. For the damping we thus obtain

$$\gamma_R = \gamma + \frac{\epsilon_P}{k_B T} \frac{N_s \omega_0^2 (\Gamma_L + \Gamma_R) f_0 (1 - f_0)}{k \left(\omega_0^2 + (\Gamma_L + \Gamma_R)^2 k^2\right)}, \tag{22}$$

with $k = 1 + (N_s - 1) f_0$. We introduced the polaronic energy $\epsilon_P = F_e^2/m\omega_0^2 = 2\hbar g^2/\omega_0$, which is the crucial energy scale of the problem. For $\omega_0 \ll \Gamma_L + \Gamma_R$ the resonance frequency simplifies to

$$\omega_Q^2 = \omega_0^2 \left[1 - \frac{\epsilon_P}{k_B T} N_s \frac{f_0(1 - f_0)}{[1 + (N_s - 1) f_0]^2} \right]. \tag{23}$$

The importance of the ratio $\epsilon_P/k_B T$ it is clearly visible here, since when this ratio is sufficiently large ω_Q^2 changes sign, indicating the appearance of a bistability. Note that f_0 is the Fermi distribution of the metal electrodes. One can readily verify that the resonance frequency associated with the linear part of the restoring force is lowest when $f_0 = 1/(1 + N_s)$. It reads

$$\omega_Q^2\big|_{\text{min}} = \omega_0^2 \left[1 - \frac{\epsilon_P}{4 k_B T} \right], \tag{24}$$

independently of N_s. Substituting the same value of $f_0 = 1/(N_s + 1)$ into the expression for the damping Eq. (22) for $\omega_0 \ll \Gamma_L + \Gamma_R$ one obtains

$$\gamma_R = \gamma + \frac{\epsilon_P}{k_B T} \frac{\omega_0^2}{4 \Gamma_{\text{e}}}, \tag{25}$$

where $\Gamma_{\text{e}} = (\Gamma_L + \Gamma_R) N_s/(N_s + 1)$. Thus in terms of Γ_{e} the expression of the damping at the maximum of reduction of the frequency does not depend on N_s. This expression has been used to extract the value of Γ_e in the main text.

D. Effective potential

The reduction of the resonance frequency is due to the back-action of the electronic system on the oscillator. This generates an effective force acting on the oscillator that depends on x in a non-linear fashion due to the x-dependence of the tunnelling rate:

$$F_{\text{eff}}(x) = -m\omega_0^2 x + F_e N_s \Gamma^+(x)/\Gamma_{\text{e}}(x). \tag{26}$$

Here $\Gamma^+(x)$ and $\Gamma_{\text{e}}(x)$ are defined in Sec. I B using $\epsilon_0 \to \epsilon_0 - F_e x$. In the equilibrium case ($eV \ll k_B T$) the force reads:

$$F_{\text{eff}}(x) = -m\omega_0^2 x + \frac{F_e}{e^{(\epsilon - F_e x)/k_B T - \ln N_s} + 1}, \tag{27}$$

where $\epsilon = \epsilon_1 - eV_g C_g/C_\Sigma$. The electronic contribution is clearly non-linear. The interpretation is simple. The force induced by the electrons is just F_e multiplied by the probability that the dot is occupied by an additional electron. In equilibrium this probability is given by the Fermi function. Note however that it does not coincide with the Fermi distribution of the metals (f_0), since the chemical potentials in the dot and in the leads differ. The number of electronic degrees of freedoms N_s appear only as a shift of the energy level. The equilibrium condition for the mechanical oscillator $F_{\text{eff}}(x_0) = 0$ gives

$$m\omega_0^2 x_0 = \frac{F_e}{e^{(\epsilon - F_e x_0)/k_B T - \ln N_s} + 1}. \tag{28}$$

The spring constant is proportional to the derivative with respect to x_0 of the right-hand side of this expression. It is maximal for

$$(\epsilon_M - F_e x_0)/k_B T = \ln N_s. \tag{29}$$

When sweeping the gate voltage, that is ϵ, the resonance frequency reaches it minimum at ϵ_M. (One can show that the energies ϵ corresponding to the maximum of the conductance and to the the maximum of the reduction of the frequency coincide only in the case of spin-less fermions $N_s = 1$; the difference in ϵ is however of the order of $k_B T \ln N_s$ and is thus difficult to resolve experimentally.) In terms of the displacement from the equilibrium value, $\tilde{x} = x - x_0$, the effective force acquires a particularly simple form:

$$F_{\text{eff}}(\tilde{x}) = -m\omega_0^2 \tilde{x} + \frac{F_e}{2} \tanh\left[\frac{F_e \tilde{x}}{2 k_B T}\right], \tag{30}$$

which becomes for small $F_e \tilde{x}/2k_B T$

$$F_{\text{eff}}(\tilde{x}) = -\left[m\omega_{\text{m}}^{\text{o}\;2} - \frac{1}{4x_{\text{zp}}^2} \frac{(\hbar g)^2}{k_{\text{B}} T} \right] \tilde{x} - \frac{1}{48 x_{\text{zp}}^4} \frac{(\hbar g)^4}{(k_{\text{B}} T)^3} \tilde{x}^3. \tag{31}$$

We can obtain from Eq. 30 the effective potential by integration:

$$U_{\text{eff}}(\tilde{x}) = \frac{m\omega_0^2 \tilde{x}^2}{2} - k_B T \ln\left[\cosh\left[\frac{F_e \tilde{x}}{2 k_B T}\right]\right], \tag{32}$$

where we choose the arbitrary potential constant such that $U_{\text{eff}}(0) = 0$. The potential is symmetric in this case [when Eq. (29) holds], the general form can be readily derived by integrating Eq. (30).

From Eq. (32) one can see that the effective potential evolves from a purely parabolic behaviour for F_e small to a double well for F_e sufficiently large. It is interesting to write the potential in terms of the dimensionless variable $z = \tilde{x}/(F_e/m\omega_0^2)$, that measures the distances in units of the displacement induced by the force F_e. The potential reads:

$$\frac{U_{\text{eff}}}{\epsilon_P} = \frac{z^2}{2} - \frac{1}{\tilde{\epsilon}_P} \ln\cosh(\tilde{\epsilon}_P z/2). \tag{33}$$

One can see that its form depends now on a single parameter $\tilde{\epsilon}_P = \epsilon_P/k_B T$, that is the natural coupling constant

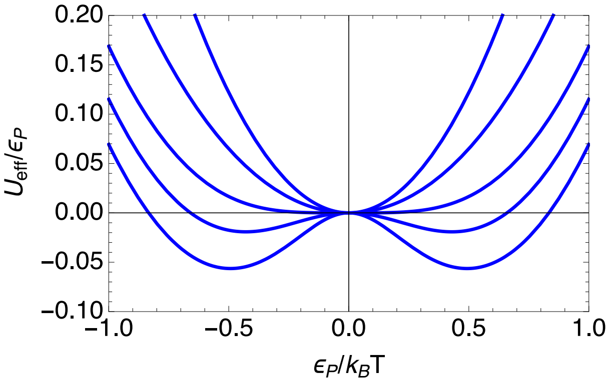

Fig. S1: Evolution of the effective potential for the oscillator for different values of the ratio $\epsilon_P/k_BT = 0.1, 2, 4, 6, 10$ from the upper to the lower curve. For $\epsilon_P/k_BT = 4$ the potential is quartic at leading order.

of the problem. We show in Fig. S1 the evolution of the potential for $\tilde{\epsilon}_P = 0.1, 2, 4, 6, 10$. One can expand the potential to order 4 to obtain:

$$\frac{U_{\text{eff}}}{\epsilon_P} = \frac{z^2}{2}\left(1 - \frac{\tilde{\epsilon}_P}{4}\right) + \frac{\tilde{\epsilon}_P^3}{192} z^4 + \dots . \tag{34}$$

For $\tilde{\epsilon}_P \ll 1$, one has a simple harmonic oscillator. For $\tilde{\epsilon}_P = 4$ the quadratic term vanishes and for small displacement the potential is quartic at leading order. For $\tilde{\epsilon}_P > 4$ the system is bistable and features a double-well potential.

The bistability is directly related to the two possible states of the dot, empty or filled with one electron. The phase diagram and the crossover to the bistability in the coherent tunnelling limit has been discussed in Refs. [8, 9]. In the bistable region the current is strongly reduced leading to a current blockade induced by the electron-phonon coupling. Recently it has been proposed to exploit this kind of bistability in a double-dot coupled to an oscillator to design a nanomechanical qubit[10].

E. Fluctuation spectrum and softening of the mechanical mode

The first effect of the coupling is a reduction of the resonance frequency. For small $\tilde{\epsilon}_P$ or for small displacement this follows from the expression of the quadratic part of the effective potential (Eq. 34) that leads to

$$\frac{\omega_Q^2}{\omega_0^2} = 1 - \frac{\tilde{\epsilon}_P}{4} \qquad \text{for } \tilde{\epsilon}_P \ll 1. \tag{35}$$

This effect has been observed by several groups [11–17]. For larger values of $\tilde{\epsilon}_P$ one cannot rely anymore on just the value of the quadratic part to quantify the observed mechanical resonance frequency. The oscillator becomes highly non-linear, so some care has to be taken to measure the resonance frequency of the system in equilibrium. This can be done by measuring the driven spectrum by keeping the driven vibration amplitude smaller than the standard deviation of the thermal vibration amplitude. Otherwise, the resonance frequency depends on the intensity of the drive used to detect it, see Sec. I G. Even for infinitesimal drive, the thermal fluctuations allow to explore regions of different vibration amplitudes for which the period of the oscillator takes values that can be very different. In order to find an averaged value for the observed resonance frequency for small drive we will follow again Ref. [8] and calculate the displacement fluctuation spectrum at equilibrium:

$$S_{xx}(\omega) = \int dt e^{i\omega t} \langle (\tilde{x}(t) - \langle \tilde{x} \rangle)(\tilde{x}(0) - \langle \tilde{x} \rangle) \rangle. \tag{36}$$

For a small coupling constant $S_{xx}(\omega)$ reduces to a Lorentzian function peaked at ω_Q as defined in Eq. (35). For a larger coupling constant the resanance peak broadens and shifts to lower frequencies, but it remains well identified, and the resonance frequency can be determined for instance, by measuring $S_{xx}(\omega)$ [18]. In Ref. [8] it is shown that in the equilibrium limit $S_{xx}(\omega)$ coincides with the response function for a weak drive, which is what is measured in this work. In equilibrium and for infinitesimal damping, $S_{xx}(\omega)$ can be calculated following the methods of statistical mechanics [19]:

$$S_{xx}(t) = \int d\tilde{x}_o dp_o P(\tilde{x}_o, p_o) \left[\tilde{x}(t)\tilde{x}(0) - \langle \tilde{x} \rangle^2 \right], \tag{37}$$

where $\tilde{x}(t)$ is the solution to the time evolution of the displacement when the force is given by F_{eff} in Eq. (30) with initial conditions for the displacement and the momentum $\tilde{x}_o$ and p_o. The quantity P is the Boltzman distribution:

$$P(\tilde{x}_o, p_o) = \mathcal{N} e^{-\frac{p_o^2/2m + U_{\text{eff}}(\tilde{x}_o)}{k_B T}} \tag{38}$$

where U_{eff} is given by Eq. (32) and $\mathcal{N}$ is a normalization factor.

In order to perform the calculation it is convenient to change the integration variables. Instead of using $(\tilde{x}_o, p_o)$ we will use (E, τ), where $E = p_o^2/2m + U(\tilde{x}_o)$ and τ is the time along the trajectory of energy E. The Jacobian is unitary $d\tilde{x}_o dp_o = dE d\tau$. We can now write the spectrum as follows:

$$S_{xx}(t) = \int dE \int_0^{T_E} d\tau_E e^{-E/k_B T} \mathcal{N} \tilde{x}_E(t + \tau_E) \tilde{x}_E(\tau_E) \tag{39}$$

where τ_E is the time along the trajectory with energy E and T_E is the period of the orbit. Note that one could have more than one orbit for a given energy. We will focus in the following on the stable case occurring when $\tilde{\epsilon}_P < 4$ and for which only one orbit is present. We can now perform the Fourier transform of Eq. (39) by introducing the Fourier series of the orbit displacement:

$$\tilde{x}_E(\tau) = \sum_{n=-\infty}^{+\infty} e^{-in\omega_E\tau}\tilde{x}_n(E) \quad (40)$$

$$\tilde{x}_n(E) = \int_0^{T_E} \frac{d\tau}{T_E} e^{in\omega_E\tau} x_E(\tau) \quad (41)$$

with $\omega_E = 2\pi/T_E$. Substituting these expressions into Eq. (39) and performing the Fourier transform we obtain:

$$S_{xx}(\omega) = \mathcal{N}\int dE e^{-E/k_BT} \sum_{n\neq 0} |\tilde{x}_n(E)|^2 T_E 2\pi\delta(\omega - n\omega_E). \quad (42)$$

Note that dropping the $n = 0$ harmonics allows to subtract the average of the trajectory.

We now perform the integral in the energy variable. The equation $n\omega_{E_n(\omega)} = \omega$ defines a function $E_n(\omega)$ for each trajectory. We can then write:

$$S_{xx}(\omega) = \mathcal{N} e^{-E_n(\omega)/k_BT} \sum_{n\neq 0} |\tilde{x}_n(E_n(\omega))|^2 \frac{2\pi n}{\omega} \frac{2\pi}{n\left|\frac{d\omega_E}{dE}\right|} \quad (43)$$

This expression can be used to compute the spectrum either numerically for any value of the parameters, or analytically in some limits. In Extended Data Fig. 1 we show the result of the numerical evalution of this expression for $\tilde{\epsilon}_P < 4$. For $\tilde{\epsilon}_P > 4$ the system becomes bistable; the crossover between the stable and the bistable regions occurs when the quadratic term of the effective potential vanishes, see the dotted yellow line in Extended Data Fig. 1. Due to the strong non-linearity of the potential combined with the thermal fluctuations, the spectrum has a maximum corresponding to the resonance frequency (thick red continuous line), which approaches $\approx 0.75\omega_0$ at $\tilde{\epsilon}_P = 4$. The spectrum in Extended Data Fig. 1 also shows a large broadening of the resonance due to phase fluctuations. The effective quality factor approaches $Q \simeq 5.5$ at $\tilde{\epsilon}_P = 4$. Note that there is no direct contribution of the dissipation to the peak broadening in the model. Taking into account the dissipation induced by the coupling between vibrations and single-electron tunneling (SET) changes only qualitatively the peak broadening in Extended Data Fig. 1.

The dependence of the maximum of this spectrum as a function of $\tilde{\epsilon}_P$ has been used in the main text (see Fig. 3d) to fit the temperature dependence of the resonance frequency at the gate voltage corresponding to the conductance peak and infer an estimate of ϵ_P. We do not have an analytical expression, but fitting the numerical result one obtains

$$\omega_M/\omega_0 = 1 + \sum_{n=1}^{5} a_n \tilde{\epsilon}_P^n \quad (44)$$

with $a_1 = -0.127655$, $a_2 = 0.010475$, $a_3 = 0.0125029$, $a_4 = -0.00480876$, and $a_5 = 0.000515142$, which is within 0.1% of the numerical result for $0 \leq \tilde{\epsilon}_P \leq 4$.

F. Coefficients of a series expansion of the potential in the displacement and estimation of the thermal energy stored in the non-harmonic part of the potential

In this section we derive explicit expressions for the first 4 coefficients of the series expansion of the effective potential for small $\tilde{x}$. We will express these nonlinear coefficients as well as the amount of thermal energy stored in the nonlinearity as a function of ϵ_P. This allows us to quantify the amount of thermal energy stored in the nonlinearity shown in Fig. 5d of the main from the suppression of the resonance frequency measured at each temperature text using Eq. 44. We will use the standard notation:

$$U_{\rm eff}(\tilde{x}) = U_0 + \frac{m\omega_Q^2}{2}\tilde{x}^2 + \frac{m\beta_D}{3}\tilde{x}^3 + \frac{m\gamma_D}{4}\tilde{x}^4. \quad (45)$$

Since the constant is irrelevant, we can obtain the other coefficients directly from the expression of the effective force Eq. (30) using $dU_{\rm eff}/dx = -F_e n + m\omega_0^2 x$, $d^2U_{\rm eff}/dx^2 = -F_e dn/dx + m\omega_0^2$, and so on. Here $n = 1/\left(\exp\{(\epsilon - F_e x)/k_BT - \ln N_s\} + 1\right)$ and has to be evaluated at $x = x_0$, that is, the equilibrium position. Using the properties of n we have:

$$\frac{\omega_Q^2}{\omega_0^2} = 1 - \frac{\epsilon_P}{k_BT} n(1-n) \quad (46)$$

$$\beta_D = \frac{F_e^3}{2m(k_BT)^2} n(1-n)(2n-1) \quad (47)$$

$$\gamma_D = -\frac{F_e^4}{6m(k_BT)^3} n(1-n)(6n^2 - 6n + 1). \quad (48)$$

We evaluate explicitly these expressions at the symmetric point for which $n = 1/2$:

$$\frac{\omega_Q^2}{\omega_0^2} = 1 - \frac{\epsilon_P}{4k_BT}, \qquad \beta_D = 0, \quad (49)$$

$$\gamma_D = \frac{F_e^4}{48m(k_BT)^3} = \frac{\epsilon_P^2 m\omega_0^4}{48(k_BT)^3}. \quad (50)$$

These expressions are independent of the value of N_s.

In order to quantify the degree of non-linearity of the potential it is interesting to compare the contribution of the average of the quadratic term of the potential to the average of the full effective potential. For this we can use the expression of the effective potential given by Eq. (33). The average value of z^2 reads:

$$\langle z^2 \rangle = \int dz e^{-U_{\rm eff}(z)/\tilde{\epsilon}_P} z^2 \Big/ \int dz e^{-U_{\rm eff}(z)/\tilde{\epsilon}_P} = 1/\tilde{\epsilon}_P + 1/4. \quad (51)$$

Thus the average of the (dimensionless) quadratic part of the potential reads:

$$U_2 \equiv \frac{d^2U_{\rm eff}}{dz^2}\left\langle\frac{z^2}{2}\right\rangle = (1-\tilde{\epsilon}_P/4)(1/\tilde{\epsilon}_P+1/4)/2. \quad (52)$$

In a similar way we can calculate the average of the full potential

$$\langle U_{\rm eff}\rangle = \int dz e^{-U_{\rm eff}(z)/\tilde{\epsilon}_P} U_{\rm eff}(z) \Big/ \int dz e^{-U_{\rm eff}(z)/\tilde{\epsilon}_P}. \quad (53)$$

The quantity $\langle U_{\rm eff}\rangle - U_2$ corresponds to the average of the sum of all the nonlinear terms of the potential, which could be interpreted as the amount of thermal energy stored in the nonlinearity. One finds numerically that $\langle U_{\rm eff}\rangle - U_2 \approx 0.0169\tilde{\epsilon}_P + 0.001\tilde{\epsilon}_P^2$ in the region $0 < \tilde{\epsilon}_P \leq 4$. This quantity is finite at $\tilde{\epsilon}_P = 4$ where U_2 vanishes. Thus, approaching this value the sum of the contribution of the non-linear terms becomes dominant with respect to the contribution of the quadratic term. A plot of $(\langle U_{\rm eff}\rangle - U_2)/U_2$ as a function of $\tilde{\epsilon}_P$ is shown in Fig. S2. $(\langle U_{\rm eff}\rangle - U_2)/U_2 \approx 0.033\tilde{\epsilon}_P^2$ for $\tilde{\epsilon}_P \to 0$ and $(\langle U_{\rm eff}\rangle - U_2)/U_2 \approx 1.34/(4-\tilde{\epsilon}_P)$ for $\tilde{\epsilon}_P \to 4$, the bistability threshold.

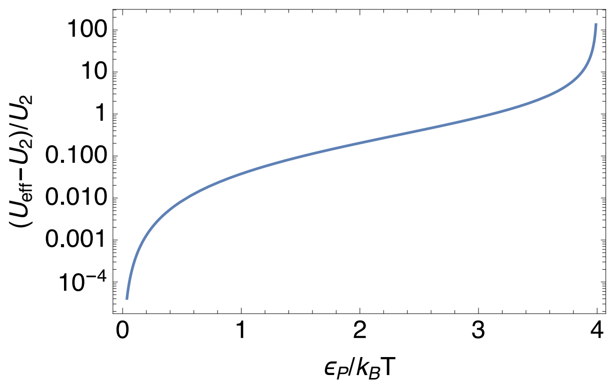

Fig. S2: Fraction of thermal energy stored in the nonlinearity, *i.e.* the ratio of the average of the sum of the nonlinear terms of the potential to the average of the quadratic part U_2.

G. Nonlinear Duffing response in presence of thermal fluctuations

In this subsection we consider the response of the nonlinear oscillator to an external drive. The results of this section are used to extract the value of the coupling g from the measurement of the shift of the resonance frequency as a function of the driven vibration amplitude in Fig. 5b of the main text and to perform the fit of the response spectrum. The measurements are performed as close as possible to the symmetric point, for which the potential is symmetric in $\tilde{x}$. We will thus focus on this symmetric point, limiting the expansion to the quartic term. This corresponds to the standard Duffing oscillator in presence of thermal fluctuations. We find that the typical thermal amplitude of fluctuations of the oscillator are sufficiently large to induce a sizable change in the resonance frequency. It is thus crucial to include these fluctuations that modify quantitatively the nonlinear response to an external drive.

We will follow standard methods to describe the system [19, 20]. For clarity and uniformity of notation, we derive the main equations that lead to a Fokker-Planck description (see Eq. (70) in the following) of the slow degrees of freedoms: the two quadratures. We begin by writing a Langevin equation for the displacement $\tilde{x}$:

$$\ddot{\tilde{x}} = -\gamma\dot{\tilde{x}} - \omega_0^2\tilde{x} - \gamma_D\tilde{x}^3 + f_D\cos(\omega t) + f_N(t), \quad (54)$$

where γ_D is the non-linear Duffing coefficient, and f_D and $f_N(t)$ are the driving and thermal forces divided by the mass. We assume

$$\langle f_N(t) f_N(t')\rangle = 2D\delta(t-t') \quad (55)$$

with $D = k_BT\gamma/m$. We now introduce the complex (quadrature) variable $z(t)$ as follows:

$$\begin{aligned}\tilde{x}(t) &= z(t)e^{i\omega t} + z(t)^* e^{-i\omega t} \quad (56)\\ \dot{\tilde{x}}(t) &= i\omega\left[z(t)e^{i\omega t} - z(t)^* e^{-i\omega t}\right]. \quad (57)\end{aligned}$$

We can now perform the derivative of the above two equations:

$$\begin{aligned}\dot{\tilde{x}}(t) &= i\omega\left[z(t)e^{i\omega t} - z(t)^* e^{-i\omega t}\right] \quad (58)\\ \ddot{\tilde{x}}(t) &= 2i\omega\dot{z}(t)e^{i\omega t} + (i\omega)^2\left[z(t)e^{i\omega t} + z(t)^* e^{-i\omega t}\right] \quad (59)\end{aligned}$$

where we have used the condition $\dot{z}(t)e^{i\omega t} + \dot{z}(t)^* e^{-i\omega t} = 0$ implicit in the definition of z. Substituting the equations for $\tilde{x}$, $\dot{\tilde{x}}$, and $\ddot{\tilde{x}}$ in the equation of motion, multipling it by $e^{-i\omega t}$, and averaging it over a period with the assumption that z evolves slowly gives

$$\begin{aligned}2i\omega\dot{z}(t) &= \omega^2 z(t) - i\gamma\omega z(t) - \omega_0^2 z(t) - 3\gamma_D|z|^2 z(t)\\ &\quad + \frac{f_D}{2} + \langle f_N(t)e^{-i\omega t}\rangle. \quad (60)\end{aligned}$$

We now introduce the time variable $\tau = \gamma t/2$ and scale z as $q(\tau) = \sqrt{3\gamma_D/\omega\gamma}\, z(2\tau/\gamma)$. This gives

$$\dot{q}(\tau) = -i\Omega q(\tau) - q(\tau) + i|q|^2 q(\tau) - iF_0 - iF_N(\tau), \quad (61)$$

where we approximated $\omega^2 - \omega_0^2 \approx 2\omega(\omega-\omega_0)$ and defined

$$\Omega = \frac{(\omega-\omega_0)}{\gamma/2}, \qquad F_0 = \frac{\sqrt{3\gamma_D}f_D}{2\,(\omega\gamma)^{3/2}}, \quad (62)$$

$$F_N(t) = \left\langle\frac{\sqrt{3\gamma_D}f_N(t)e^{-i\omega t}}{(\omega\gamma)^{3/2}}\right\rangle. \quad (63)$$

Neglecting the fluctuations, the stationary solution reads

$$q_0 = F_0/(|q_0|^2 - \Omega + i). \quad (64)$$

This defines the usual Duffing response. In particular one can express the dimensionless resonance frequency as a function of the amplitude:

$$\Omega = |q_0|^2 \pm \sqrt{F_0^2/|q_0|^2 - 1}. \tag{65}$$

The first term defines what is called the 'back-bone' of the resonance. This corresponds roughly to the dependence of the maximum of the amplitude oscillation on the driving frequency when measuring the spectra for different drives. It depends quadratically on the dimensionless oscillation amplitude. When the thermal fluctuations are negligible this dependence can be used to extract the value of the non-linear Duffing coefficient from the data. We discuss in the following the validity of this relation in presence of large thermal fluctuations.

We can now introduce $q = u + iv$, with u and v real. We have then

$$\dot{u} = g_u(u,v) + \xi_u(\tau), \qquad \dot{v} = g_v(u,v) + \xi_v(\tau), \tag{66}$$

with

$$\xi_u + i\xi_v = -i\sqrt{3\gamma_D}\left\langle f_N(t)e^{i\omega t}\right\rangle / (\omega\gamma)^{3/2}. \tag{67}$$

and

$$g_u = -u-(u^2+v^2-\Omega)v, \qquad g_v = -v+(u^2+v^2-\Omega)u-F_0. \tag{68}$$

The correlation functions of the ξ-fields can be approximated by $\langle\xi_u(\tau)\xi_v(\tau')\rangle = 0$, $\langle\xi_u(\tau)\xi_u(\tau')\rangle = \langle\xi_v(\tau)\xi_v(\tau')\rangle = 2\mathcal{D}\delta(\tau-\tau')$ where

$$\mathcal{D} = \frac{3\gamma_D D}{4\omega^3\gamma^2} = \frac{3\gamma_D k_B T}{4m\omega^3\gamma}. \tag{69}$$

Finally from the two Langevin equations for u and v we can derive a Fokker-Planck equation for the probability $W(u,v)$:

$$\mathcal{D}(\partial_u^2 + \partial_v^2)W - \partial_u(g_u W) - \partial_v(g_v W) = \partial_t W. \tag{70}$$

The Fokker-Planck Eq. (70) can be solved numerically for a given set of parameters to obtain the function

$$q_0(F_0,\mathcal{D},\Omega) = u_0+iv_0 = \int dudv\, W(u,v)(u+iv). \tag{71}$$

This gives the average of the two quadratures in dimensionless units.

As a first application of this equation we calculate numerically the maximum of the response amplitude of the oscillator $|q_0^{\max}|$ and the value $\Omega_{\max}$ for which this maximum appears. When fluctuations are negligible, for $\mathcal{D} \to 0$, from Eq. (65) one has $\Omega_{\max} = |q_0^{\max}|^2$. In Fig. S3 we plot $\Omega_{\max}$ as a function of $|q_0^{\max}|$ for different values of $\mathcal{D}$. For the smallest value of $\mathcal{D} = 0.1$ a good parabolic behavior is observed. Increasing $\mathcal{D}$ the curves flatten and deviations from the simple quadratic behavior are visible.

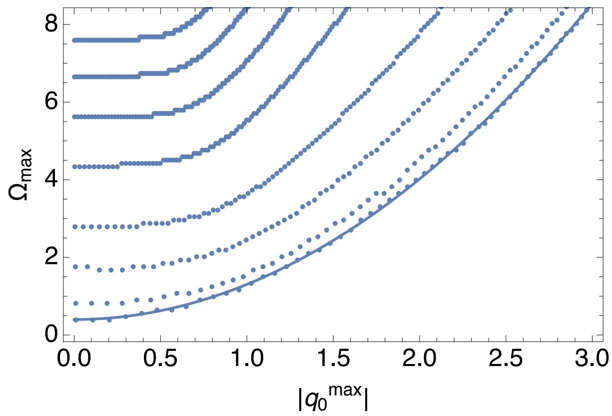

Fig. S3: The Figure shows $\Omega_{\max}$ as a function of $|q_0^{\max}|$ for $\mathcal{D} = .1, .2, .5, 1., 2., 3., 4., 5.$, from the lower to the upper curve. The effect of the fluctuations is to shift the initial value to higher frequency and to deform the dependence on $|q_0^{\max}|$. In the case of $\mathcal{D} = .1$ we show a fit with a quadratic dependence that gives a coefficient of $0.9|q_0^{\max}|^2$. The small steps are due to the discretization of the frequency in the numerical calculation.

This shows that using the quadratic dependence of the back-bone to extract the Duffing coefficient gives a qualitatively reasonable result when $\mathcal{D} < 1$. In order to have a more reliable estimate, in the next subsection we discuss a fitting procedure that exploits the form of the response spectrum as predicted by the Fokker-Planck approach.

H. Procedure used to fit the nonlinear Duffing response

Using the results described in the previous sub-section, we now explain the procedure to determine the Duffing constant, and thus the ratio ϵ_P/k_BT and the coupling g, from driven nonlinear spectra when the thermal fluctuations are large. These data are shown in Figs. 5a,c in main text and Fig. S4. We obtain the Duffing constant by collectively fitting the whole set of measured spectra spanning the linear-nonlinear crossover when sweeping the drive intensity. The spectra are measured nearby the conductance peak, that is, almost at the symmetric point. From the experimentally measured spectra, the two quadratures $\{U_{ni}, V_{ni}\}$ are extracted for N_v different values of the driving gate voltage V_n^{ac} and for N_w different values of the driving frequency ω_{ni} One has thus a set of $2N_vN_w$ values with $N_v = 10$ and $N_n = 300$. Using the expression of the nonlinear coefficient given by Eq. (50) and the definition of $\mathcal{D}$ given by Eq. (69) we can write a dimensionfull expression of the quadratures $\{u_e, v_e\}$:

$$u_e = \frac{1}{\tilde{\epsilon}_P}\sqrt{\frac{k_BT\gamma}{m\omega_0^3}}u_0(F_0, \tilde{\epsilon}_P^2\omega_0/64\gamma, (2\omega-\omega_0)/\gamma), \tag{72}$$

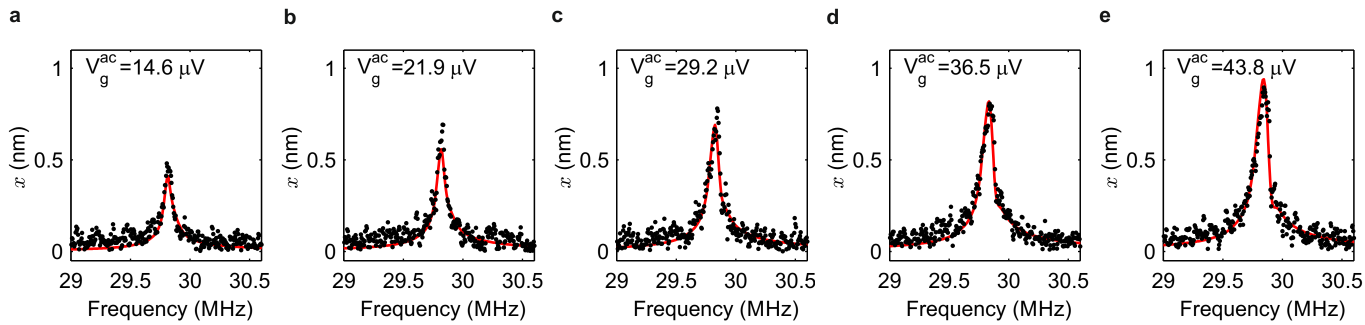

Fig. S4: Driven nonlinear spectra spanning the linear-nonlinear crossover when increasing the drive at 6 K. We emphasize that a single set of parameters is used to fit the data of 10 different spectra; the fit is shown by the red line.

$$v_e = \frac{1}{\tilde{\epsilon}_P}\sqrt{\frac{k_B T\gamma}{m\omega_0^3}}v_0(F_0, \tilde{\epsilon}_P^2\omega_0/64\gamma, (2\omega-\omega_0)/\gamma). \quad (73)$$

Here $u_0(F_0, \mathcal{D}, \Omega)$ and $v_0(F_0, \mathcal{D}, \Omega)$ are the (average of the) dimensionless quadratures obtained from the solution of the Fokker-Planck equation as defined by Eq. (71). We then define the χ^2 function:

$$\chi^2 = \sum_{n=1}^{N_v}\sum_{i=1}^{N_w}\Big[\left(u_e(\omega_{ni}, F_0 = F_v V_n^{ac}) - U_{ni}\right)^2 + \left(v_e(\omega_{ni}, F_0 = F_v V_n^{ac}) - V_{ni}\right)^2\Big]. \quad (74)$$

The free parameters of the fit are $\{\omega_0, \gamma, \tilde{\epsilon}_P, F_v\}$. The factor F_v is the relation between the dimensionless driving force intensity and the experimental driving voltage. This only assumes that the driving force increases linearly with the amplitude of the injected ac drive. The best fit for $V_g^{dc} = 0.7572$ V gives the values $\epsilon_P/k_BT = 0.22$, $\omega_0/2\pi = 29.7696$ MHz, $\gamma/2\pi = 13.229$ kHz, $F_v = 2.10897 \cdot 10^5$ V^{-1}. The fit is shown in Fig. S4.

In order to determine the error bar of the estimated value of ϵ_P/k_BT, we find numerically the minimum of χ^2 for a given value of ϵ_P/k_BT by tuning the other three parameters ω_0, γ, and F_v (see Fig. S5). We estimate this error by finding the range in ϵ_P/k_BT for which $\chi^2(\epsilon_P) < 1.5\chi^2_{\min}$, where $\chi_{\min}$ is the minimum value of χ^2. The value of 1.5 is chosen so that the probability of observing a χ^2 larger that this value is less than 1%. We find $0.15 < \epsilon_P/k_BT < 0.32$, which converts into a ± 120 MHz error in the estimation of g. In addition to this error, one should include the imprecision in the calibration of the displacement, since the fit is very sensitive to the absolute value of the displacement. By performing the fit with different values of the displacement calibration, we found that $\Delta\epsilon_P/k_BT \approx 0.15\Delta A/A$, where ΔA is the systematic error in the measurement of the displacement amplitude. We estimate $\Delta A/A = 0.22$, which gives an additional ± 0.033 to the error bar for ϵ_P/k_BT (and ± 97 MHz error for $g/2\pi$). Overall, we get the coupling constant $g/2\pi = 646 \pm 217$ MHz.

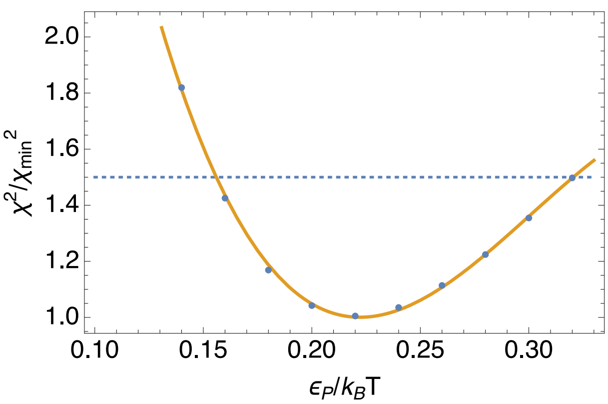

Fig. S5: Dependence of the χ^2 on ϵ_P/k_BT.

II. EXPERIMENTAL SECTION

A. Detection of mechanical vibrations and estimation of the effective mass

We use a new two-source mixing method to measure the spectral mechanical response of driven vibrations in the linear and the nonlinear regimes. This method enables us to extract the spectral mechanical response by eliminating the inherent contribution of pure electrical origin in electrical mixing measurements [21]. We detect the vibrations by capacitively driving them with an oscillating voltage with amplitude V_g^{ac} and frequency ω, applying the oscillating voltage with amplitude V_g^{ac} with a slightly detuned frequency $\omega + \delta\omega$ on the source electrode, and measuring the current at frequency $\delta\omega$ from the drain electrode. To improve the sensitivity of the current detection, we connect the drain electrode to a RLC resonator placed nearby the device and a HEMT amplifier at the 4 K stage of the dilution cryostat [22]. The RLC resonator enables us to measure the current at a comparatively high frequency $\delta\omega \simeq 1.2$ MHz where the $1/f$ noise is significantly reduced. Without the induc-

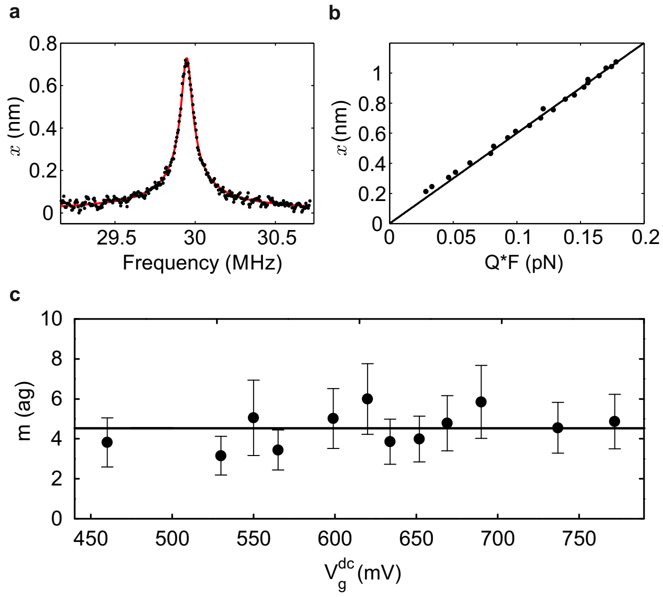

Fig. S6: Determination of the effective mass. (a) Spectral response of the displacement amplitude of the driven vibrations at $T = 6$ K. We chose the gate voltage close to the half maximum of the conductance peak, where the transconduction is largest. The red solid line is the fit of the data to a Lorenzian peak. (b) Force-displacement response curve at the mechanical resonance frequency. (c) Effective modal mass measured at different gate voltages. The black solid line indicates the average effective mass of 4.5 ag. The confidence interval error bars arise primarily from the uncertainty in the determination of the dot-gate separation.

tance L of the RLC resonator, the frequency $\delta\omega$ has to be set to a lower frequency, typically $1-10$ kHz, within the bandwidth imposed by the resistance of the sample and the capacitance of the electrical cables that connect the device to the measurement instruments. To obtain the spectral mechanical response of driven vibrations, we separate the signal of the mechanical vibrations from the signal of pure electrical origin inherent to the mixing method by properly tuning the phase of the measured current [21]. This is important since the measured current is otherwise a non-trivial combination of the vibration displacement and the electrical contribution. The pure electrical contribution is used as a resource to calibrate the signal of the vibrations into units of meters. Figure S6a shows the spectral response of driven vibrations, which can be well described by a Lorentzian peak.

The effective mass of the measured mechanical eigenmode can be reliably determined, since the driven vibration amplitude can be calibrated with the two-source mixing method described above and since the capacitive force in quantum dot electromechanical devices can be accurately quantified. The mass m is quantified from the slope of the force-displacement (F-x) response at the mechanical resonance frequency in Fig. S6b using $x = (Q/m\omega_{\mathrm{m}}^2)F$ where the quality factor Q is estimated from the spectral response in Fig. S6a and the capacitive force is given by

$$F = \beta C_{\mathrm{g}}' V_{\mathrm{g}}^{\mathrm{dc}} V_{\mathrm{g}}^{\mathrm{ac}}, \tag{75}$$

$$\beta = 1 - \frac{C_{\mathrm{g}}}{C_\Sigma} + f(1-f)\frac{C_{\mathrm{g}}}{C_\Sigma}\frac{e^2/C_\Sigma}{k_{\mathrm{B}}T}, \tag{76}$$

in the incoherent SET regime [21]. The dot-gate capacitance C_{g}, the total capacitance C_Σ of the dot, and the average charge occupation number f (with value between 0 and 1) are all quantified by standard electron transport measurements. The spatial derivative of the dot-gate capacitance C_{g}' is determined from C_{g} and the dot-gate separation d using the expression of the capacitance between a cylinder and a plate that leads to $C_{\mathrm{g}}' = C_{\mathrm{g}}/d\ln(2d/r)$. Figure S6c shows the effective mass measured at twelve different conductance peaks. The average effective mass is $m = 4.5 \pm 1.5$ ag. The uncertainty in the mass determination comes from the mass fluctuations in Fig. S6c and the uncertainty in the estimation of the dot-gate separation. We estimate the nanotube radius $r = 1.5$ nm from the measured mass and the suspended nanotube length determined by scanning electron microscopy. This value is consistent with the radii of the nanotubes produced with our chemical vapour deposition growth.

B. Electromechanical coupling and electron tunnel rate

Figures S7a-h show the temperature dependence of both the resonance frequency and the resonance width of driven vibrations measured at the conductance peaks for different gate voltages. The fitting of these data to the predictions of the theory enable us to determine the coupling g and the total electron tunnel rate Γ_{e} for these different conductance peaks. The values of g and Γ_{e} are shown in Figs. 4a,c of the main text. In the fitting we only select the black data points in Figs. S7a-d with resonance frequency ratios $\omega_{\mathrm{dip}}/\omega_{\mathrm{m}}^{\mathrm{o}}$ between 0.75 and 1, since it is the range of values expected by the predictions discussed in Sec. I E. The grey data points correspond to data at lower temperature where a double-well potential is expected to emerge, but further work in needed to characterize this regime. The coupling of vibrations and SET also results in dissipation. The mechanical resonance width in the high temperature limit ($k_{\mathrm{B}}T \gg \hbar g^2/\omega_{\mathrm{m}}$) is given by

$$\Delta\omega = \Gamma_0 + \frac{1}{2}\frac{\hbar g^2}{k_{\mathrm{B}}T}\frac{\omega_{\mathrm{m}}^{\mathrm{o}}}{\Gamma_{\mathrm{e}}} \tag{77}$$

where Γ_0 is the damping due to other dissipation mechanisms, see Eq. 25. We fit the measured resonance width in the high temperature limit with Eq. 77 in Fig. S7e-h. The electron tunnel rates Γ_{e} obtained from the fits are shown in Fig. 4c of the main text.

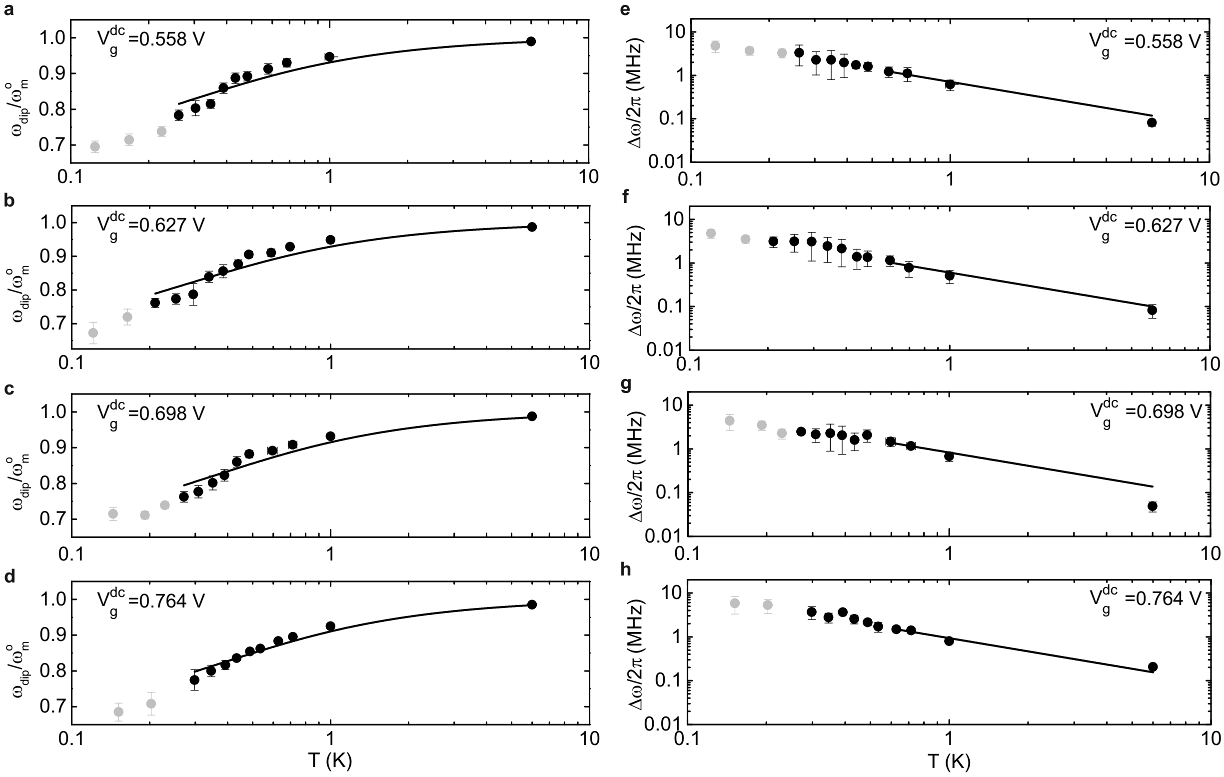

Fig. S7: Determination of the electromechanical coupling and the electron tunnel rate. (a)-(d) Temperature dependence of the mechanical resonance frequency $\omega_{\rm dip}$ for different conductance peaks. We define $\omega_{\rm dip}$ as the lowest resonance frequency when sweeping the gate voltage over a conductance peak (Fig. 3b of main text). The gate voltage of the resonance frequency dip matches the gate voltage of the conductance peak. The black solid lines indicate the SET-based predictions. (e)-(h) Temperature dependence of the mechanical resonance width for different conductance peaks. The black solid lines indicate the SET-based predictions in the high temperature limit. The confidence interval error bars in panels (a)-(d) and (e)-(h) arise primarily from the uncertainty in the fit of the measured temperature dependence of $\omega_{\rm m}$ and $\Delta\omega$, respectively, to the predictions of the theory.

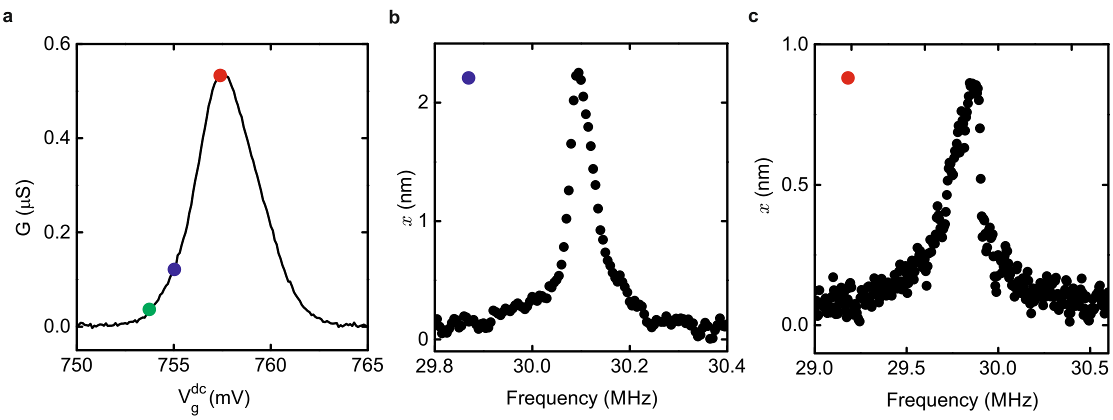

Fig. S8: Spring hardening and softening in the nonlinear spectral response of mechanical vibrations in Device I at 6 K. (a) Gate voltage dependence of the conductance. (b) Nonlinear response showing spring softening when the system is set at the base of the conductance peak (blue point). (c) Nonlinear response showing spring hardening when the system is set at the top of the conductance peak (red point).

C. Nonlinear spectral response of mechanical vibrations

We show here that the nonlinear Duffing constant measured at 6 K changes sign when sweeping the gate voltage through the conductance peak, in agreement with the predictions of the theory in Sec. I F. This enables us to rule out other possible origins for the nonlinearity, such as the geometrical nonlinearity [23]. We observe both a softening and hardening spring behaviour of the oscillator over a narrow range in gate voltage, see Figs. S8a-c. Figure S8c shows the spectral response of the spring hardening when the system is set at the conduction peak as indicated by the red dot in Fig. S8a. By contrast, Fig. S8b shows the spring softening effect at the base of the conductance peak as highlighted by the blue dot in Fig. S8a. The change of the nonlinear Duffing sign is consistent with the predictions of the theory describing the coupling of mechanical vibrations and SET in the incoherent regime. Indeed, Eq. 48 indicates that the Duffing constant is positive at the conductance peak when the average charge occupation fraction $f = 1/2$, while it becomes negative at the base of the peak when f is sufficiently close to zero.

D. Responsivity of mechanical vibrations

We show that the observed reduction of the responsivity at large drive is related to the thermal switching between coexisting stable states in driven nonlinear oscillators. Figures S9a,b show the drive dependence of both the mechanical resonance frequency and the responsivity of the mechanical vibrations when the system is set at the very base of the conductance peak, see green dot in Fig. S8a.

We do not observe any shift in resonance frequency, indicating that the Duffing constant is becoming small. This is expected from Eq. 48 when $f \simeq 0$, that is, when the effect of the coupling between vibrations and SET is suppressed. We do not observe any change of the responsivity either, showing that nonlinear damping plays a negligible effect [24].

By contrast, Fig. S9d shows that the responsivity gets lower when increasing the drive in the case where the system is set at the top of the conductance peak, see red dot in Fig. S8a. This reduction is well reproduced by the SET-based predictions (Fig. 5c in main text), which relates this behaviour to switching between coexisting stable states in driven nonlinear oscillators, and not to nonlinear damping.

E. Strong anharmonicity in two other devices

We demonstrate strong anharmonicity and ultrastrong coupling regime in two other devices. Figure S10a shows a conduction peak of Device II. The charging energy, the level spacing, and the electron tunnel rate are $E_c = 14$ meV, $\Delta E = 2$ meV, and $\hbar\Gamma_e = 2$ μeV, respectively, showing that SET is in the incoherent regime ($\hbar\Gamma_e < k_B T < \Delta E, E_c$). The high lever arm $\alpha = 0.83$ arises from the short separation between the nanotube and the gate electrode. Figure S10b shows a dip with a large suppression of the mechanical resonance frequency when sweeping the gate voltage through the conductance peak; the bare resonance frequency is $\omega_m^o/2\pi = 35.1$ MHz. Figure S10c shows the temperature dependence of the mechanical resonance frequency at the dip. The ratio ω_{dip}/ω_m^o approaches 0.75 at low temperature, indicating that the potential of the vibrations becomes strongly anharmonic. The red solid line is the fit of the data to the SET-based predictions, enabling us to quantify $g/2\pi = 384$ MHz. This value is similar to the value $g/2\pi = 395$ MHz obtained with independently measured parameters and using $g = e(C_g'/C_\Sigma)V_g^{dc}/\sqrt{2m\hbar\omega_m^o}$. These data indicate that the device is in the ultrastrong coupling ($g > \omega_m^o$) and the adiabatic regime ($\Gamma_e > \omega_m^o$), which satisfy the conditions to realize strong vibration anharmonicity. Figures S10d-f show the data of Device III. We obtain $g/2\pi = 529$ MHz and $\omega_m^o/2\pi = 89$ MHz, which shows that device is in the ultrastrong coupling regime. The measured suppression of the resonance frequency ω_{dip}/ω_m^o reaches 0.93 at

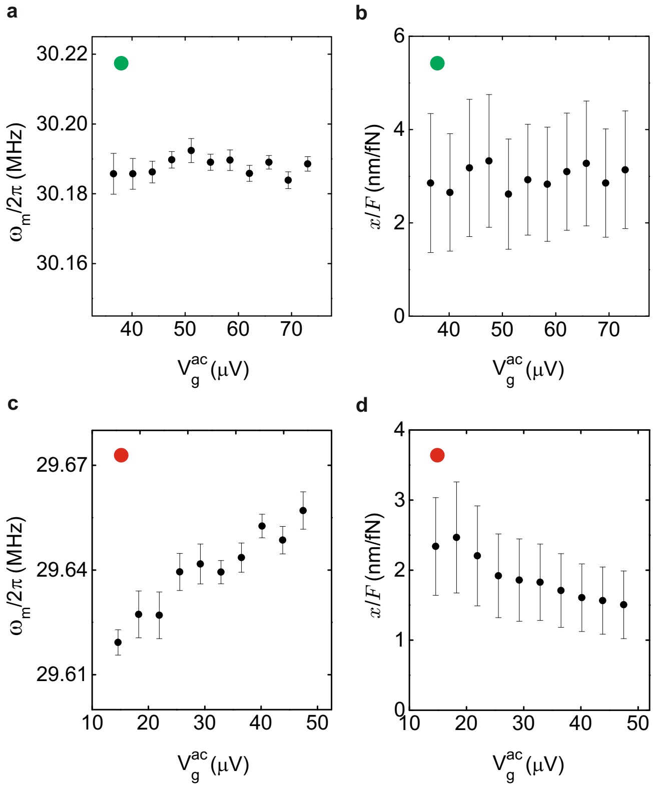

Fig. S9: Responsivity of mechanical vibrations at 6 K. (a,b) Resonance frequency and responsivity of the vibrations as a function of the driving voltage with the system set at the very base of the conductance peak in Fig. S8a (green dot). (c,d) Same as (a,b) but with the system set on the top of the conduction peak (red dot). The confidence interval error bars in (a,c) and (b,d) arise from the uncertainty in the fitting of the spectral response and the determination of the dot-gate separation, respectively.

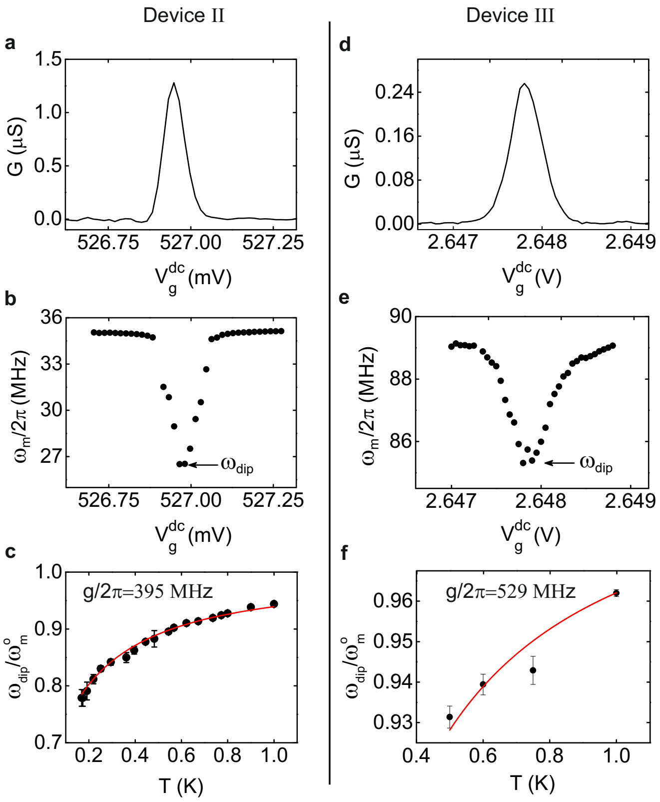

Fig. S10: Strong anharmonicity and ultra-strong coupling regime in two other devices. (a,b) Conductance and mechanical resonance frequency as a function of gate voltage at 170 mK for Device II. (c) Suppression of the resonance frequency as a function of temperature at the conduction peak. The solid red line is the SET-base prediction. (d,e) Conductance and mechanical resonance frequency as a function of gate voltage at 6 K for Device III. (f) Suppression of the resonance frequency as a function of temperature at the conduction peak. The confidence interval error bars in panels (c) and (f) arise primarily from the standard deviation in ω_{m} quantified from different driven spectral response measurements.

500 mK. The device could not be measured at lower temperature due to technical problems unrelated to the device itself. The anharmonicity is sizeable but not as large as that in Devices I and II.

F. Parameters of Device I discussed in the main text

Parameters	Device I
Suspended nanotube length (L)	1.2 μm
Nanotube radius (r)	1.5 nm
Effective mechanical mode mass (m)	4.5 ag
Bare resonance frequency ($\omega_{\mathrm{m}}^{\mathrm{o}}/2\pi$)	28.3-30.3 MHz
Nanotube-gate separation (d)	150 nm
Zero point fluctuation (x_{zp})	7.9 pm
Nanotube-gate capacitance (C_g)	9.7 aF
Lever arm (α)	$0.4 - 0.5$
Charging energy (E_c)	$8.5 - 6.5$ meV
Level spacing (ΔE)	$0.97 - 0.73$ meV
Work function difference between nanotube and gate	120 mV

G. Literature review: estimation of $x_{\mathrm{nl}}/x_{\mathrm{zp}}$

Here we describe how we estimate the ratio $x_{\mathrm{nl}}/x_{\mathrm{zp}}$ for each device shown in Fig. 1 of the main text. Figure S11 shows the same figure but with an identification number for each device.

Device 1 is a double-clamped single-wall carbon nanotube resonator [25]. The resonance frequency is $\omega_{\mathrm{m}}^{\mathrm{o}} = 2\pi \times 46.35$ MHz. The amplitude $x_{\mathrm{nl}} = 4.2$ nm is obtained from the section X in the supplementary information (SI) of Ref. [25]. We estimate the effective mass $m \approx 13.3$ ag from the geometry of the nanotube. The device is measured at 60 K.

Device 2 is a levitated silica nanoparticle with 100 nm diameter [26]. The mass is $m \approx 1$ fg. The resonance frequency of the mode along the optical axis z is $\omega_{\mathrm{m}}^{\mathrm{o}} = 2\pi \times 77.6$ kHz. The device is cooled down to an average phonon occupation of 0.65 quanta. The mechanical linewidth $\Delta\omega = 2\pi \times 11.1$ kHz is obtained from the solid line in Fig. 2a. The amplitude x_{nl} is obtained from

$$x_{\mathrm{nl}} = \sqrt{\frac{8}{3\sqrt{3}} \frac{\Delta\omega\omega_{\mathrm{m}}^{\mathrm{o}}}{\gamma}} \tag{78}$$

We estimate $x_{\mathrm{nl}} = 103.3$ nm from Eq. (78) using the value of $\gamma = 4.9 \times 10^{24}$ m^{-2}s^{-2} found in Ref. [27].

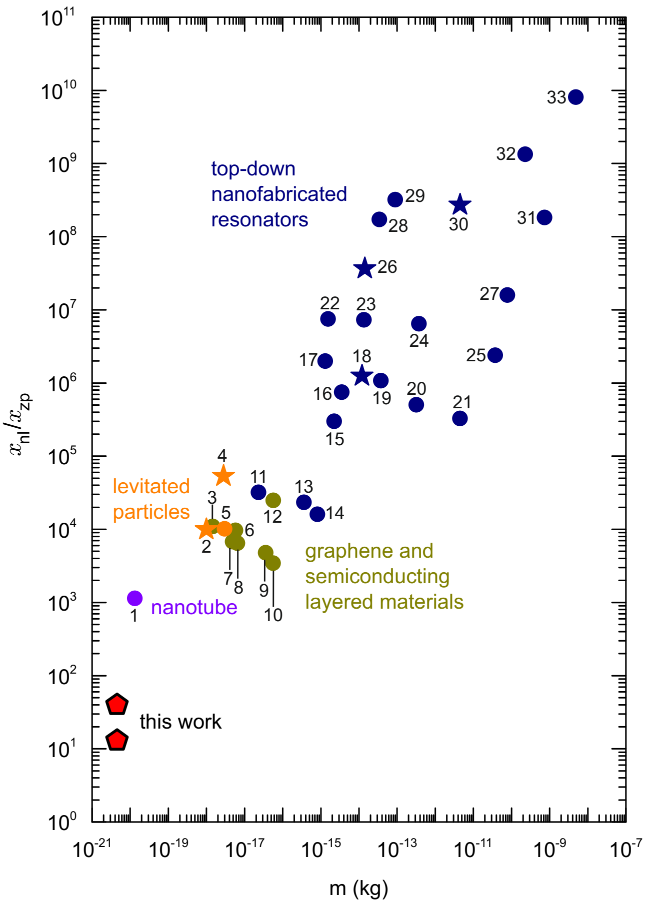

Fig. S11: Same figure as Fig. 1 of the main text but with the identification number of each device.

Device 3 is a single-layer drum-head molybdenum disulfide (MoS_2) resonator [28]. The resonance frequency is $\omega_m^o = 2\pi \times 28.5$ MHz. The amplitude $x_{nl} = 4.9$ nm is obtained from Fig. 4A. We estimate the effective mass $m \approx 1.5$ fg from the geometry of the device. The device is measured at room temperature.

Device 4 is a levitated silica nanoparticle with 71.5 nm radius [29]. The mass is $m \approx 2.8$ fg. The resonance frequency of the mode along the optical axis z is $\omega_m^o = 2\pi \times 104$ kHz. The device is cooled down to an average phonon occupation of 0.56 quanta. The decoherence rate due to backaction and residual gas molecules is $\Gamma = 2\pi \times 19.4$ kHz. The Duffing constant $\gamma = 2.67 \times 10^{24}$ m^{-2}s^{-2} is obtained from section D in the SI in Ref. [29]. We estimate the amplitude $x_{nl} = 286.1$ nm using Eq. (78).

Device 5 is a levitated silica nanoparticle with 75 nm diameter [27]. The mass of the resonator is $m \approx 3$ fg. The resonance frequency of the mode along the optical axis x is $\omega_m^o = 2\pi \times 125$ kHz. The amplitude $x_{nl} = 48$ nm is obtained from Fig. S3c in the SI of Ref. [27].

Device 6 is a single-layer drum-head MoS_2 resonator [30]. The resonance frequency is $\omega_m^o = 2\pi \times 30.5$ MHz. The amplitude $x_{nl} \approx 2.1$ nm is obtained from Fig. 5b using the displacement–to–voltage conversion in the section S3 of the SI. We estimate the effective mass $m \approx 5.8$ fg from the geometry of the device. The device is measured at room temperature.

Device 7 is a double-clamped graphene resonator [31]. The resonance frequency is $\omega_m^o = 2\pi \times 65$ MHz. The amplitude $x_{nl} = 1.1$ nm is obtained from Fig. 2d. The effective mass $m \approx 4.9$ fg is obtained from Fig. 3a (Device 1). The device is measured at room temperature.

Device 8 is a double-clamped bi-layer MoS_2 resonator [32]. The resonance frequency is $\omega_m^o = 2\pi \times 54$ MHz. The amplitude $x_{nl} = 1.0$ nm is obtained from Fig. S3c. The effective mass $m \approx 6.5$ fg is obtained from Table S2 (Device 1) in the SI. The device is measured at room temperature.

Device 9 is a drum-head graphene resonator [33]. The resonance frequency is $\omega_m^o = 2\pi \times 33.3$ MHz. The amplitude $x_{nl} = 0.4$ nm is obtained from Fig. 5a. The effective mass $m \approx 36.0$ fg is obtained from Fig. 3e. The device is measured at 30 mK.

Device 10 is a drum-head graphene resonator [34]. The resonance frequency is $\omega_m^o = 2\pi \times 44$ MHz. The amplitude $x_{nl} = 0.2$ nm is obtained from Fig. S13. The effective mass $m \approx 56.0$ fg is obtained from Table S1 (Device II) in the SI. The device is measured at 15 mK.

Device 11 is a double-clamped platinum nanowire resonator [35]. The resonance frequency is $\omega_m^o = 2\pi \times 45.35$ MHz. The amplitude $x_{nl} = 2.68$ nm is obtained from the main text. The effective mass $m \approx 23.2$ fg is estimated from the geometry of the device. The device is measured at 20 K.

Device 12 is a drum-head 5 nm thick graphene resonator [36]. The resonance frequency is $\omega_m^o = 2\pi \times 14.7$ MHz. The amplitude $x_{nl} = 2.5$ nm is obtained from Fig. 1b. The effective mass $m \approx 56.4$ fg is estimated from the geometry of the device. The device is measured at room temperature.

Device 13 is a double-clamped silicon carbide (SiC) beam resonator [37]. The resonance frequency is $\omega_m^o = 2\pi \times 8.78$ MHz. The amplitude $x_{nl} = 1.2$ nm is obtained from Fig. 2 at $V_g^{dc} = 0$. The effective mass $m \approx 0.36$ pg is estimated from the geometry of the device. The device is measured at room temperature.

Device 14 is a double-clamped palladium beam resonator [38]. The resonance frequency is $\omega_m^o = 2\pi \times 20.26$ MHz. The amplitude $x_{nl} = 0.36$ nm is obtained from Fig. 2B (iii). The effective mass $m \approx 0.81$ pg is estimated from the geometry of the device (sample B1). The device is measured at 1 K.

Device 15 is a double-clamped silicon nitride (SiN) beam resonator [39]. The resonance frequency is $\omega_m^o = 2\pi \times 6.53$ MHz. The mechanical linewidth $\Delta\omega = 2\pi \times 20$ Hz is obtained from Fig. S3b. The value of Duffing constant $\gamma = 1.54 \times 10^{26}$ m^{-2}s^{-2} is obtained from Eq. S39 in the SI. We estimate the amplitude $x_{nl} = 7.2$ nm using Eq. (78).The effective mass $m \approx 2.23$ pg is estimated from the geometry of the device. The device is measured at room temperature.

Device 16 is a double-clamped beam resonator patterned from a four-layer stack of aluminum nitride (AlN)-molybdenum (Mo)-AlN-Mo [40]. The resonance frequency is $\omega_{\rm m}^{\rm o} = 2\pi \times 14.31$ MHz. The amplitude $x_{\rm nl} = 9.6$ nm is obtained from Fig. 1d. The effective mass $m \approx 3.5$ pg is estimated from the geometry of the device. The device is measured at room temperature.

Device 17 is a goal-post shaped silicon resonator [41]. The resonance frequency is $\omega_{\rm m}^{\rm o} = 2\pi \times 7.1$ MHz. The amplitude $x_{\rm nl} = 60$ nm is obtained from Fig. 2. The effective mass $m \approx 1.3$ pg is taken from the main text. The device is measured at 4.2 K.

Device 18 is a aluminium drum-head resonator [42]. The resonance frequency is $\omega_{\rm m}^{\rm o} = 2\pi \times 15.1$ MHz. The device is cooled down to an average phonon occupation of 0.3 quanta. The mechanical linewidth $\Delta\omega = 2\pi \times 400$ Hz is obtained from Fig.1. The value of Duffing constant $\gamma = 5.05 \times 10^{27}$ m^{-2}s^{-2} is obtained from Ref. [43] for a similar drum resonator. We estimate the amplitude $x_{\rm nl} = 8.5$ nm using Eq. (78). The effective mass $m \approx 12$ pg is estimated from the geometry of the device. The device is measured at 0.5 mK.

Device 19 is a double-clamped SiN beam resonator [44]. The resonance frequency is $\omega_{\rm m}^{\rm o} = 2\pi \times 0.64$ MHz. The amplitude $x_{\rm nl} = 20$ nm is obtained from Fig. 1c. The effective mass $m \approx 37.6$ pg is estimated from the geometry of the device. The device is measured at 5 K.

Device 20 is a drum-head resonator made from a superconducting alloy of Molybdenum and Rhenium (MoRe) [45]. The resonance frequency is $\omega_{\rm m}^{\rm o} = 2\pi \times 7.29$ MHz. The amplitude $x_{\rm nl} = 0.95$ nm is obtained from Fig. 4.4a (yellow curve) in Ref. [46]. The effective mass $m \approx 0.32$ ng is estimated from the geometry of the device given in the SI. The device is measured at 20 mK.

Device 21 is a soft clamped SiN membrane patterned with a phononic crystal structure resonator [47]. The resonance frequency is $\omega_{\rm m}^{\rm o} = 2\pi \times 1.46$ MHz. The mechanical linewidth $\Delta\omega \approx 2\pi \times 1.8$ mHz is obtained from Fig. 4b. The value of Duffing constant $\gamma = 1.15 \times 10^{24}$ m^{-2}s^{-2} is obtained from Eq. 10 and Fig. 2b in the main text. We estimate the amplitude $x_{\rm nl} = 0.37$ nm using Eq. (78). The effective mass $m \approx 4.5$ ng is taken from the Ref. [48]. The device is measured at room temperature.

Device 22 is a polycrystalline silicon cantilever resonator [49]. The resonance frequency is $\omega_{\rm m}^{\rm o} = 2\pi \times 1.5$ MHz. The amplitude $x_{\rm nl} = 450$ nm is obtained from Fig. 6. The effective mass $m \approx 1.55$ pg is estimated from the geometry of the device. The device is measured at room temperature.

Device 23 is a double-clamped SiN beam resonator [50]. The resonance frequency is $\omega_{\rm m}^{\rm o} = 2\pi \times 0.66$ MHz. The device is externally driven by Gaussian noise force. The variance of the displacement noise $\Delta x_1^2 = 5 \times 10^{-14}$ m^2 is taken from the first data point in the inhomogeneous broadening regime (IB) in Fig. 3a. We estimate $x_{\rm nl} = \sqrt{\Delta x_1^2} = 224$ nm. The effective mass $m \approx 13.5$ pg is estimated from the geometry of the device.

Device 24 is a meshed SiN membrane resonator [51]. The resonance frequency is $\omega_{\rm m}^{\rm o} = 2\pi \times 4.13$ MHz. The amplitude $x_{\rm nl} = 15$ nm is estimated theoretically in the paper. This value is very close to the experimentally observed results shown in Fig. 4c and 5a. The linear spring constant k = 253 N/m is obtained from the paper. We estimate the effective mass $m = {\rm k}/{\omega_{\rm m}^{\rm o}}^2 = 37.6$ ng. The device is measured at room temperature.

Device 25 is a commercially available SiN membrane resonator from Norcada Inc [52]. The resonance frequency is $\omega_{\rm m}^{\rm o} = 2\pi \times 133.8$ kHz. The amplitude $x_{\rm nl} = 3.1$ nm is obtained from the inset of Fig. 2. The effective mass $m \approx 37.5$ ng is estimated from the geometry of the device. The device is measured at room temperature.

Device 26 is a aluminium drum-head resonator [53]. The resonance frequency is $\omega_{\rm m}^{\rm o} = 2\pi \times 13.0$ MHz. The device is cooled down to an average phonon occupation of 0.38 quanta. The mechanical linewidth is obtained from Fig. 2e. We use Eq. S31 and Eq. S32 to estimate the mechanical linewidth $\Delta\omega = 2\pi \times 331$ kHz. We estimate $x_{\rm nl} = 245$ nm from Eq. (78) using the value of $\gamma = 4.35 \times 10^{27}$ m^{-2}s^{-2} found in Ref. [43] for a drum resonator. The effective mass $m \approx 14.3$ pg is estimated from the geometry of the device.

Device 27 is a double-clamped GaAs resonator membrane resonator [54]. The resonance frequency is $\omega_{\rm m}^{\rm o} = 2\pi \times 138$ kHz. The amplitude $x_{\rm nl} \approx 14$ nm is obtained from Fig. 1c and using the voltage to displacement conversion ≈ 70 nm/μV. The effective mass $m \approx 78$ ng is estimated from the geometry of the device. The device is measured at 4.2 K.

Device 28 is a SiN cantilever resonator [55]. The resonance frequency is $\omega_{\rm m}^{\rm o} = 2\pi \times 951$ kHz. The amplitude $x_{\rm nl} = 2.75$ μm is obtained from Fig. 3c. The effective mass $m \approx 34.4$ pg is estimated from the geometry of the device. The device is measured at room temperature.

Device 29 is a SiN cantilever resonator [55]. The resonance frequency is $\omega_{\rm m}^{\rm o} = 2\pi \times 150$ kHz. The amplitude $x_{\rm nl} = 8$ μm is obtained from Fig. 3d. The effective mass $m \approx 89.5$ pg is estimated from the geometry of the device. The device is measured at room temperature.

Device 30 is a soft clamped SiN membrane patterned with a phononic crystal structure resonator [56]. The resonance frequency is $\omega_{\rm m}^{\rm o} = 2\pi \times 1.14$ MHz. The device is cooled down to an average phonon occupation of 0.3 quanta. The effective mechanical linewidth $\Delta\omega = 2\pi \times 2$ kHz is obtained from the blue data points in Fig. 4a. We estimate $x_{\rm nl} = 347$ nm from Eq. (78) using the value of $\gamma = 1.15 \times 10^{24}$ m^{-2}s^{-2} found in Ref. [47]. The effective mass $m \approx 4.5$ ng is taken from the Ref. [48].

Device 31 is a highly doped polycrystalline silicon plate resonator [57]. The resonance frequency is $\omega_{\rm m}^{\rm o} = 2\pi \times 73$ kHz. The mechanical linewidth $\Delta\omega = 2\pi \times 0.31$ Hz is obtained from Fig. 3b. The value of Duffing constant $\gamma = 2.64 \times 10^{20}$ m^{-2}s^{-2} is obtained from the main text. We estimate $x_{\rm nl} = 72.2$ nm from Eq. (78). The effective mass $m \approx 0.7$ μg is estimated from the geometry of the device. The device is measured at room temperature.

Device 32 is a SiN membrane resonator [58]. The resonance frequency is $\omega_{\mathrm{m}}^{\mathrm{o}} = 2\pi \times 188.1$ kHz. The amplitude $x_{\mathrm{nl}} = 0.59$ μm is obtained from Fig. 2d. The effective mass $m \approx 0.23$ μg is estimated from the geometry of the device. The device is measured at room temperature.

Device 33 is a goal-post shaped Si resonator [59]. The resonance frequency is $\omega_{\mathrm{m}}^{\mathrm{o}} = 2\pi \times 1.9$ kHz. The mechanical linewidth $\Delta\omega = 2\pi \times 40$ mHz and the Duffing constant $\gamma = 7.9 \times 10^{13}$ $\mathrm{m}^{-2}\mathrm{s}^{-2}$ are obtained from Fig. 3b. We estimate the amplitude $x_{\mathrm{nl}} = 7.64$ μm using Eq. (78). The effective mass $m \approx 4.9$ μg is obtained from fig. 2d. The device is measured at 4.0 K.

[1] L. I. Glazman and M. Pustilnik, in *New Directions in Mesoscopic Physics (Towards Nanoscience)*, edited by R. Fazio, V. F. Gantmakher, and Y. Imry (Springer Netherlands, Dordrecht, 2003), pp. 93–115, ISBN 978-1-4020-1665-3 978-94-007-1021-4.

[2] A. D. Armour, M. P. Blencowe, and Y. Zhang, Phys. Rev. B **69**, 125313 (2004), ISSN 1098-0121, 1550-235X.

[3] Y. M. Blanter, O. Usmani, and a. Y. V. Nazarov, Phys. Rev. B. **93**, 136802 (2004), ISSN 0031-9007, 1079-7114.

[4] Y. M. Blanter, O. Usmani, and a. Y. V. Nazarov, Phys. Rev. Lett. **94**, 049904 (2005), ISSN 0031-9007, 1079-7114.

[5] D. Mozyrsky, M. B. Hastings, and I. Martin, Phys. Rev. B **73**, 035104 (2006), ISSN 1098-0121, 1550-235X.

[6] F. Pistolesi and S. Labarthe, Phys. Rev. B **76**, 165317 (2007), ISSN 1098-0121, 1550-235X.

[7] A. Benyamini, A. Hamo, S. V. Kusminskiy, F. von Oppen, and S. Ilani, Nat. Phys. **10**, 151 (2014), ISSN 1745-2473, 1745-2481.

[8] G. Micchi, R. Avriller, and F. Pistolesi, Phys. Rev. Lett. **115**, 206802 (2015), ISSN 0031-9007, 1079-7114.

[9] G. Micchi, R. Avriller, and F. Pistolesi, Phys. Rev. B **94**, 125417 (2016), ISSN 2469-9950, 2469-9969.

[10] F. Pistolesi, A. N. Cleland, and A. Bachtold, Phys. Rev. X **11**, 031027 (2021).

[11] B. Lassagne, Y. Tarakanov, D. Kinaret, J.and Garcia-Sanchez, and A. Bachtold, Science **325**, 1107 (2009).

[12] G. A. Steele, A. K. Hüttel, B. Witkamp, M. Poot, H. B. Meerwaldt, L. P. Kouwenhoven, and H. S. J. van der Zant, Science **325**, 1103 (2009).

[13] A. Benyamini, A. Hamo, S. V. Kusminskiy, F. von Oppen, and S. Ilani, Nature Physics **10**, 151 (2014).
[14] I. Khivrich, A. A. Clerk, and S. Ilani, Nature Nanotechnology **14**, 161 (2019), ISSN 1748-3395.
[15] C. Urgell, W. Yang, S. L. De Bonis, C. Samanta, M. J. Esplandiu, Q. Dong, Y. Jin, and A. Bachtold, Nat. Phys. **16**, 32 (2020).
[16] Y. Wen, N. Ares, F. J. Schupp, T. Pei, G. A. D. Briggs, and E. A. Laird, Nat. Phys. **16**, 75 (2020).
[17] S. Blien, P. Steger, N. Híttner, R. Graaf, and A. K. Húttel, Nature Communications **11**, 1636 (2020), ISSN 2041-1723, URL https://doi.org/10.1038/s41467-020-15433-3.
[18] J. Moser, J. Güttinger, A. Eichler, M. J. Esplandiu, D. E. Liu, M. I. Dykman, and A. Bachtold, Nature Nanotechnology **8**, 493 (2013), ISSN 1748-3387, 1748-3395.
[19] M. I. Dykman and M. A. Krivoglaz, Physica A: Statistical Mechanics and its Applications **104**, 480 (1980), ISSN 0378-4371.
[20] M. I. Dykman and M. A. Krivoglaz, Soviet. Phys. JETP **50**, 30 (1979).
[21] C. Samanta, D. A. Czaplewski, S. L. De Bonis, C. B. Moller, R. T. Queralt, C. S. Miller, Y. Jin, F. Pistolesi, and A. Bachtold, arXiv preprint, arXiv:2207.02291 (2022).
[22] S. L. de Bonis, C. Urgell, W. Yang, C. Samanta, A. Noury, J. Vergara-Cruz, Q. Dong, Y. Jin, and A. Bachtold, Nano Lett. **18**, 5324 (2018), ISSN 1530-6984.
[23] A. Bachtold, J. Moser, and M. Dykman, Reviews of Modern Physics **94**, 045005 (2022).
[24] R. Lifshitz and M. C. Cross, Reviews of nonlinear dynamics and complexity **1** (2008).
[25] A. Eichler, M. del Álamo Ruiz, J. A. Plaza, and A. Bachtold, Physical review letters **109**, 025503 (2012).
[26] F. Tebbenjohanns, M. L. Mattana, M. Rossi, M. Frimmer, and L. Novotny, Nature **595**, 378 (2021).
[27] J. Gieseler, L. Novotny, and R. Quidant, Nature physics **9**, 806 (2013).
[28] J. Lee, Z. Wang, K. He, R. Yang, J. Shan, and P. X.-L. Feng, Science advances **4**, eaao6653 (2018).
[29] L. Magrini, P. Rosenzweig, C. Bach, A. Deutschmann-Olek, S. G. Hofer, S. Hong, N. Kiesel, A. Kugi, and M. Aspelmeyer, Nature **595**, 373 (2021).
[30] R. Yang, S. E. H. Yousuf, J. Lee, P. Zhang, Z. Liu, and P. X.-L. Feng, Nano Letters **22**, 5780 (2022).
[31] C. Chen, S. Rosenblatt, K. I. Bolotin, W. Kalb, P. Kim, I. Kymissis, H. L. Stormer, T. F. Heinz, and J. Hone, Nature nanotechnology **4**, 861 (2009).
[32] C. Samanta, N. Arora, and A. Naik, Applied Physics Letters **113**, 113101 (2018).
[33] P. Weber, J. Guttinger, I. Tsioutsios, D. E. Chang, and A. Bachtold, Nano letters **14**, 2854 (2014).
[34] J. Güttinger, A. Noury, P. Weber, A. M. Eriksson, C. Lagoin, J. Moser, C. Eichler, A. Wallraff, A. Isacsson, and A. Bachtold, Nature nanotechnology **12**, 631 (2017).
[35] I. Kozinsky, H. C. Postma, O. Kogan, A. Husain, and M. L. Roukes, Physical review letters **99**, 207201 (2007).
[36] D. Davidovikj, F. Alijani, S. J. Cartamil-Bueno, H. S. van der Zant, M. Amabili, and P. G. Steeneken, Nature Communications **8**, 1253 (2017).
[37] I. Kozinsky, H. C. Postma, I. Bargatin, and M. Roukes, Applied Physics Letters **88**, 253101 (2006).
[38] S. Kumar, S. Rebari, S. P. Pal, S. S. Yadav, A. Kumar, A. Aggarwal, S. Indrajeet, and A. Venkatesan, Nano Letters **21**, 2975 (2021).
[39] J. S. Huber, G. Rastelli, M. J. Seitner, J. Kölbl, W. Belzig, M. I. Dykman, and E. M. Weig, Physical Review X **10**, 021066 (2020).
[40] L. G. Villanueva, R. B. Karabalin, M. H. Matheny, E. Kenig, M. C. Cross, and M. L. Roukes, Nano letters **11**, 5054 (2011).
[41] E. Collin, T. Moutonet, J.-S. Heron, O. Bourgeois, Y. M. Bunkov, and H. Godfrin, Journal of Low Temperature Physics **162**, 653 (2011).
[42] D. Cattiaux, I. Golokolenov, S. Kumar, M. Sillanpää, L. Mercier de Lépinay, R. Gazizulin, X. Zhou, A. Armour, O. Bourgeois, A. Fefferman, et al., Nature communications **12**, 6182 (2021).
[43] D. Cattiaux, X. Zhou, S. Kumar, I. Golokolenov, R. Gazizulin, A. Luck, L. M. de Lépinay, M. Sillanpää, A. Armour, A. Fefferman, et al., Physical Review Research **2**, 033480 (2020).
[44] K. Y. Fong, W. H. Pernice, and H. X. Tang, Physical Review B **85**, 161410 (2012).
[45] S. Yanai, V. Singh, M. Yuan, M. Gely, S. J. Bosman, and G. Steele, Applied Physics Letters **110**, 083103 (2017).
[46] S. Yanai, Coherence and nonlinearity in mechanical and josephson superconducting devices, **Thesis, TU Delft** (2018).
[47] L. Catalini, M. Rossi, E. C. Langman, and A. Schliesser, Physical Review Letters **126**, 174101 (2021).
[48] Y. Tsaturyan, A. Barg, E. S. Polzik, and A. Schliesser, Nature nanotechnology **12**, 776 (2017).
[49] N. Kacem, J. Arcamone, F. Perez-Murano, and S. Hentz, Journal of Micromechanics and Microengineering **20**, 045023 (2010).
[50] O. Maillet, X. Zhou, R. Gazizulin, A. M. Cid, M. Defoort, O. Bourgeois, and E. Collin, Physical Review B **96**, 165434 (2017).
[51] E. Romero, N. P. Mauranyapin, T. M. Hirsch, R. Kalra, C. G. Baker, G. I. Harris, and W. P. Bowen, arXiv preprint arXiv:2206.11661 (2022).
[52] B. Zwickl, W. Shanks, A. Jayich, C. Yang, A. Bleszynski Jayich, J. Thompson, and J. Harris, Applied Physics Letters **92**, 103125 (2008).
[53] J.-M. Pirkkalainen, E. Damskägg, M. Brandt, F. Massel, and M. A. Sillanpää, Physical Review Letters **115**, 243601 (2015).
[54] I. Mahboob and H. Yamaguchi, Nature nanotechnology **3**, 275 (2008).
[55] L. Villanueva, R. Karabalin, M. Matheny, D. Chi, J. Sader, and M. Roukes, Physical Review B **87**, 024304 (2013).
[56] M. Rossi, D. Mason, J. Chen, Y. Tsaturyan, and A. Schliesser, Nature **563**, 53 (2018).
[57] L. Huang, S. Soskin, I. Khovanov, R. Mannella, K. Ninios, and H. B. Chan, Nature communications **10**, 3930 (2019).
[58] T. Manzaneque, M. K. Ghatkesar, F. Alijani, M. Xu, R. A. Norte, and P. G. Steeneken, arXiv preprint arXiv:2205.11903 (2022).
[59] E. Collin, Y. M. Bunkov, and H. Godfrin, Physical Review B **82**, 235416 (2010).